crystals

MDPI

Article

Crystallization of Calcium Carbonate and Calcium Phosphate Phases in Silica Hydrogel: Morphological and Compositional Characterization

Nuria Sánchez-Pastor [1,*], André Jorge Pinto [1,*], Pablo del Buey Fernández [1,2] and José Manuel Astilleros [1,3]

[1] Departamento de Mineralogía y Petrología, Facultad de Ciencias Geológicas, Universidad Complutense de Madrid, Ciudad Universitaria, 28040 Madrid, Spain; pablodelbuey@ucm.es (P.d.B.F.); jmastill@ucm.es (J.M.A.)
[2] Departamento de Mineralogía y Petrología, Facultad de Ciencias, Campus Fuente Nueva, Universidad de Granada, 18071 Granada, Spain
[3] Instituto de Geociencias Consejo Superior de Investigaciones Científicas and Universidad Complutense de Madrid, 28040 Madrid, Spain
* Correspondence: nsanchez@ucm.es (N.S.-P.); andrejor@ucm.es (A.J.P.)

Abstract: The present study showcases a series of crystallization experiments using a specially designed double diffusion system to grow crystals belonging to the calcium carbonate–phosphate system. The experimental U-shaped device comprised two vertical solution containers, separated by a horizontal column of silica hydrogel. Each container was filled with 0.5 M $CaCl_2$ and 0.5 M Na_2CO_3 solutions, which diffused through the gel column over time. Na_3PO_4 solutions, with 50 and 500 ppm concentrations, were incorporated into the gel in different experiments, resulting in a homogeneous distribution of phosphate concentrations within the diffusion column. After 15- and 30-day incubation periods post-nucleation, the crystals formed in different sections of the gel were carefully extracted and studied with scanning electron microscopy and electron microprobe. Additionally, Raman spectra were collected from the samples using a confocal Raman microscope, providing further insights into their molecular composition and structural properties. The obtained results show that under the induced experimental conditions (i) phosphate incorporates into calcite's structure, and (ii) the growth of calcium phosphates in the presence of carbonate ions involves the sequential, heterogeneous nucleation of CO_3-bearing OCP/HAP-like phases, with Raman spectral characteristics very similar to those of bioapatites.

Keywords: gel experiments; crystals growth; spectroscopy; phosphate; calcium carbonate; morphology; additive; octacalcium phosphate; bioapatite

Citation: Sánchez-Pastor, N.; Pinto, A.J.; del Buey Fernández, P.; Astilleros, J.M. Crystallization of Calcium Carbonate and Calcium Phosphate Phases in Silica Hydrogel: Morphological and Compositional Characterization. *Crystals* **2024**, *14*, 635. https://doi.org/10.3390/cryst14070635

Academic Editor: Jolanta Prywer

Received: 19 June 2024
Revised: 30 June 2024
Accepted: 6 July 2024
Published: 10 July 2024

1. Introduction

The interest in calcium carbonate precipitation is considerable, both in its importance in biomineralization and its several industrial applications. Natural calcium carbonate polymorphs, calcite and aragonite, play a central role in the global cycle of carbon [1]. Due to the fast weathering rates and high buffer capacity associated with the carbonate system, small amounts of $CaCO_3$ may strongly control the geochemical behavior of aquatic systems. The reaction of natural waters with carbonate minerals also exerts an important impact on the chemistry of the atmosphere and oceans, through the interplay established between oceanic acidity levels and atmospheric CO_2 solubility [2]. In this framework, calcite is considered a potentially important sink for both anions and cations, due to its reactive nature and ubiquity in groundwater aquifers. Several studies [3–7] regarding the mobility of environmentally relevant anions and cations have therefore focused on the adsorption and co-precipitation with calcite. In general, the role played by foreign ions in the crystallization of minerals relates to the interplay among several factors, ranging from structural incorporation into a growing solid, to adsorption onto specific surface sites [8]. It

has been demonstrated that under high supersaturation conditions, foreign ions can easily incorporate into the structure of solids, but in a higher proportion than predicted merely by thermodynamic considerations [9]. Furthermore, such deviation is strongly favored by isomorphic substitutions.

Co-precipitation experiments involving calcite and trace ions have shown that its crystal lattice tolerates the incorporation of different ions in the crystal structure. As the latter are often of contrasting ionic radius and charge with respect to Ca and CO_3, the incorporation of the trace ions often leads to structural distortion. Cations are substituted for Ca in the calcite lattice, as for example observed for Cu, Co, Cd, Mg, Zn, Pb and Ba [10–14], whereas anions are substituted for the CO_3^{2-} group, as for example observed for CrO_4^{2-} [15], SeO_4^{2-} [16].

Aqueous phosphorous (P) occurs in most natural waters in the form of phosphate (PO_4^{3-}) [17,18], which is crucial for certain biomineralization processes, and a common compound in soils and aquatic sediments. In agricultural activities, phosphates are widely used as fertilizers in large scale operations. Nevertheless, the combination of soil erosion and the release of P-rich wastewaters to the environment has led to increasing phosphate concentrations in both freshwater aquifers as well as in the oceans [19]. The result has been the ongoing hypertrophication of freshwaters and the coastal marine environment, with the subsequent degradation of water quality and the onset of toxic algae blooms. The disturbance of the terrestrial P cycle by human activity requires a proper understanding of the chemical processes regulating aqueous phosphate concentrations, in order to predict future anthropogenic effects [19]. One of the mechanisms controlling the bioavailability and mobility of phosphorus in the environment are the sorption/de-sorption mechanisms involving soils and sediments. The uptake of phosphate by minerals may proceed via adsorption (the coordination of the anion to the mineral surface), co-precipitation (the anion is substituted for lattice ions, and is thus incorporated into the mineral structure) and the precipitation of phosphate-bearing phases [20]. Frequently, natural phosphate is present in low concentrations, thus preempting precipitation. In such cases, adsorption is instead the initial step, after which the co-precipitation or formation of solid solutions may occur.

The link between calcium phosphate and carbonate systems is of special relevance to the investigation of biomineralization processes, especially those involving bioapatites. These non-stoichiometric materials may include several types of impurities (Mg, Na, K, CO_3, etc.), whose physiologically controlled concentrations determine the mechanical properties and reactivity of each kind of hard tissue (i.e., dentin, bone, enamel). A compelling summary of the crystal-chemical characteristics of bioapatites, alongside their possible reactive pathways, is provided by [21]. Within the broad field of biologically produced calcium phosphates, the study of octacalcium phosphate (OCP) has also garnered significant interest due to its critical role in biomineralization mechanisms, and its potential applications in biomedical fields, particularly hard-tissue regeneration. OCP, chemically defined as $Ca_8(HPO_4)_2(PO_4)_4{\cdot}5H_2O$, is a compound recognized for its precursor role in the formation of biological apatites, such as bone and tooth enamel. This phase is primarily characterized by a triclinic crystallographic structure, hence triclinic OCP (t-OCP) [22]. This form of OCP is defined by a specific chemical composition and structural typology, which have been extensively studied and documented in [23–25], and references therein. However, several other OCP-like phases, with similar compositions but differing structures, have also been identified, including apatitic OCP (ap-OCP), amorphous OCP (am-OCP), and carbonated OCP. Each of these phases exhibits unique properties and potential applications, particularly in the field of biomaterials [22,26,27]. Many studies have identified the crucial role of octacalcium phosphate (OCP), characterized by its water-rich composition, in the early stages of bone mineralization, acting as a transient precursor of hydroxyapatite (HAP) under physiological conditions [23,28–31]. This transformation is facilitated by the epitactic relationship between the structures of OCP and HAP, where the nuclei of the former provide a template for the crystal growth of the latter. The formation of OCP-HAP

mixtures involves several mechanisms, with epitactic growth being a key process, where the structural similarity between the (100) planes of OCP and HAP allows for a seamless transition [32–36].

Since numerous biomineralization processes occur in gelatinous matrices, the characteristics of reactant transport in hydrogels make them a suitable media to feasibly reproduce the crystallization conditions encountered in geo-biological environments [37–39]. Moreover, the possibility of preparing gels with different contents of foreign ions, their stability in a wide range of temperatures and the induced high degree of supersaturation [40–42] enables the use of these nanoporous media to grow crystals, incorporating significant amounts of foreign ions.

The present investigation focuses on the analysis and discussion of the morphological, structural, and chemical changes undergone by carbonate and phosphate crystals, grown in different silica gel media, by means of micro-Raman spectroscopy and electron microprobe studies. The obtained results show that: (i) phosphate incorporates into the calcite structure under our experimental conditions, and (ii) the growth of calcium phosphates in the presence of carbonate ions, involves the sequential, heterogeneous nucleation of CO_3-bearing OCP/HAP-like phases with Raman spectral characteristics very similar to those of bioapatites.

2. Materials and Methods

The crystallization experiments were performed in a double diffusion system consisting of two vertical branches separated by a column of silica hydrogel. The vertical branches were filled with 0.5 M $CaCl_2$ and 0.5 M Na_2CO_3 solutions, which diffused through the gel column over time. Na_3PO_4 solutions, with 50 and 500 ppm concentrations, were incorporated into the gel in different experiments, resulting in a homogeneous distribution of phosphate concentrations within the diffusion column. The silica hydrogel column was 125 mm long and 9 mm in diameter. The gel was prepared by adding 1 N HCl to a sodium silicate solution (Na_2SiO_3) (Merck KGaA, sp. gr.: 1.059 g/cm^3; pH = 11.2) until pH = 5.5 was reached. The use of these concentrations is fairly standard in diffusion–reaction experiments. Given that the timing of the first precipitates is significantly influenced by the boundary conditions of the systems, employing relatively high concentrations of $CaCl_2$ and Na_2CO_3 ensures that a sufficiently high level of supersaturation is achieved within the system. This level is sufficient to promote $CaCO_3$ crystallization within a reasonable time frame without reaching catastrophic levels, as would occur in precipitation from free solutions. This is attributed to the slow diffusivity of the ions through the porous silica gel, which ensures that the ion concentrations at the time of nucleation are much lower. Upon starting the experiments, the reactants are brought together by diffusion through the gel and, subsequently, nucleation and crystal growth occurs by chemical reaction within the gel column. Crystal growth was monitored by optical microscopy. The experiments, performed in triplicate, were stopped after two different time periods: 15 days and 1 month after the initial nucleation, and the crystals were extracted by dissolving the gel in a 1 M NaOH solution. All experiments were carried out at 25 °C. Crystals with representative morphologies were hand-picked and characterized using Raman spectroscopy, scanning electron microscopy, and electron microprobe (EMPA analysis and EDXS mapping).

Raman spectra of the samples were collected using a confocal Thermo Fischer DXR Raman spectrometer equipped with a confocal microscope, with a point-and-shoot Raman capability of one micron spatial resolution. This microscope belongs to the National Museum of Natural Sciences from Madrid (Spain). The objective selected was of 10×, together with a laser source of 532 nm at 10 mV in a laser mode power at 100%. The average spectral resolution of the Raman shift, ranging from 70 to 3300 cm^{-1}, was 2–4 cm^{-1}, i.e., grating 900 lines/mm and a spot size of 2 μm. The system was operated using OMNIC 1.0 software, adapted to working conditions such as a pinhole aperture of 25 μm and a bleaching time of 1–2 s, as well as four exposures averaged in time of 12 s each. Peak deconvolution was carried out using the software package Fityk (Version 1.3.1) [43].

To study the crystal morphologies and the textural characteristics, the samples were coated in carbon and inspected with a SEM microscope (JEOL JSM 6400, 40 kV) equipped with an EDX microanalysis detector (INCA systems). The idealized shape of the calcite crystal was modeled with the KrystalShaper software package (JCrystalSoft, Version 1.5.0) [44].

Carbon-coated polished samples were used for the microprobe measurements. The samples were analyzed for Ca and P elements using a Jeol JXA 8900 microprobe. The spot analyses were carried out with an acceleration voltage of 15 kV, a probe current of 10 nA and a defocused beam with a diameter of 5 μm. The distribution maps for major elements were measured with a dwell time of 5 ms at a beam time current of 20 nA at 10 kV. The SEM images and EMP analyses were taken at the Microscopy Centre of the Complutense University of Madrid (Spain).

3. Results

3.1. Solid Morphologies

3.1.1. Inert Silica Gel Growth Experiments

In the absence of phosphate (mixture I in Table 1) the waiting time for the first nuclei to precipitate in the gel was 216 h (measured from when the solutions were placed in the U-tube). One month after nucleation time, we observed precipitates exhibiting three different morphologies: (a) rhombohedral single crystals, bounded by rough faces depressed in their central region (hopper-like habit), and whose morphology is compatible with the {1014} form of the calcite (Figure 1a); (b) flat flower-like aggregates that consist of fan-shaped crystallites (Figure 1b); and (c) radial aggregates consisting of acicular crystallites (Figure 1c). The size of the crystals/aggregates ranged between 200–500 μm. The rhombohedral crystals are significantly more abundant than those of the flower-like and radial morphologies.

Table 1. Concentrations of the solutions used in the gel experiments.

Mixture	Reagents		GEL	Tw [1]	Morphologies
	[$CaCl_2$]	[Na_2CO_3]	[Na_2PO_4]		
I	0.5 M	0.5 M	-	216 h	Rhombohedral Flower-like Radial
II	0.5 M	0.5 M	50 ppm	216 h	Elongated
III	0.5 M	0.5 M	500 ppm	168 h 360 h	Spheres Elongated

[1] Tw: waiting time for the first nucleation.

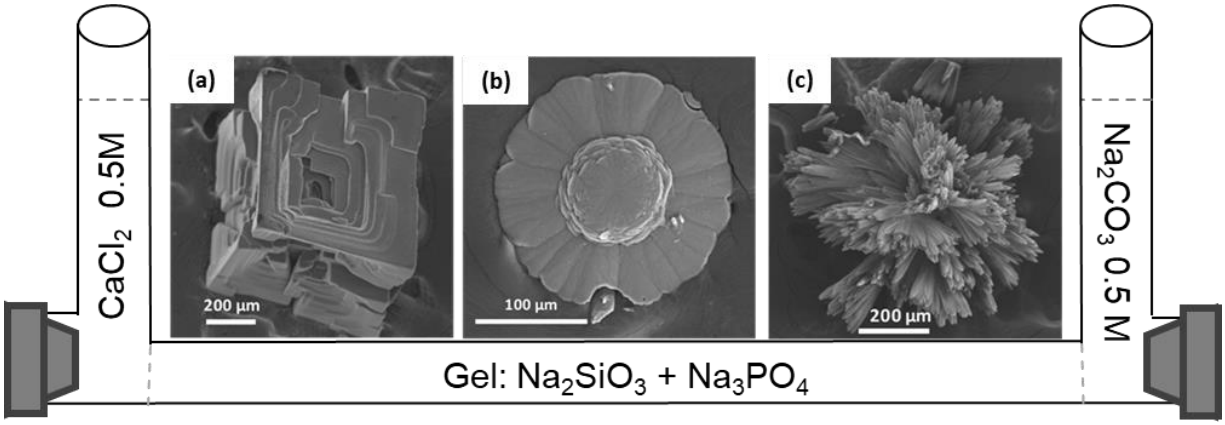

Figure 1. Experimental set-up used to grow the crystals and crystals obtained in the reference P-free experiment (Mixture I). (**a**) Rhombohedral single crystal, (**b**) flower-like aggregates and (**c**) radial aggregates of acicular crystallites.

3.1.2. The 50 ppm P-Bearing Silica Gel Growth Experiments

In growth experiments using a low amount of Na_2PO_4 (Table 1, mixture II), the waiting time for the first nuclei to precipitate was also ~216 h. In these experiments, we only observed elongated crystals with a faint blocky habit, characterized by the emergence of rounded pseudofacets slightly misoriented between each crystal (Figure 2a). This habit is mainly controlled by a more acute rhombohedron. Such crystals have also a slight but appreciable cleft in the equatorial region. The morphology of these crystals is comparable with a calcite crystal elongated along [001], bounded by the acute {0221} rhombohedron and bi-terminated by the {1014} form (Figure 2c). These habits are typical of calcite crystals grown in the presence of certain impurities [15,16,40,45].

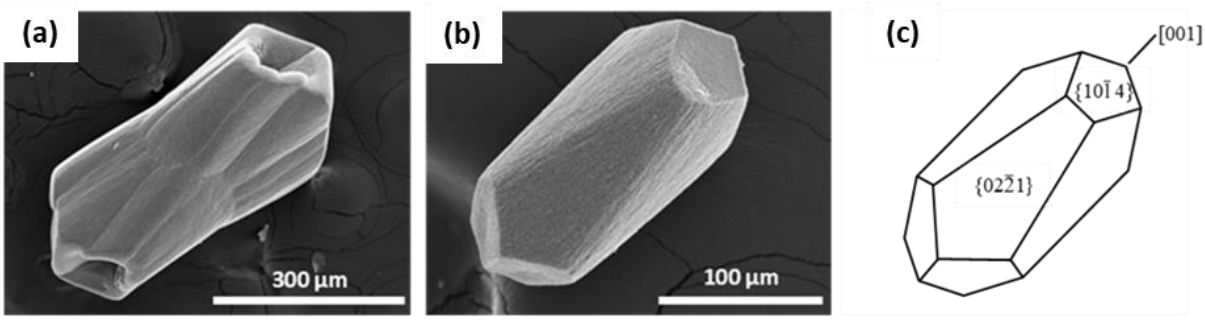

Figure 2. Crystals obtained in the P-doped experiments (**a**,**b**): (**a**) elongated crystals from Mixture II grown in the presence of 50 ppm of phosphate in the gel medium, and (**b**) elongated crystals from Mixture III grown in the presence of 500 ppm of phosphate. (**c**) Sketch showing a calcite crystal elongated along the c axis and bounded by the {0221} and {1014} rhombohedra.

3.1.3. The 500 ppm P-Bearing Silica Gel Growth Experiments

In the growth experiments using high concentrations of Na_2PO_4 (Table 1, mixture III), it was possible to distinguish two different nucleation events. The first occurred ~168 h after pouring the reagents into the branches of the tubes, while the second nucleation event occurred after 360 h. The precipitates formed in the first event showed spherical morphologies. Figure 3 displays the SEM images of these solids, removed from the gel after 15 days (Figure 3a,c) and one month (Figure 3b,d) after the first nuclei appeared. Though the precipitates obtained are spherical in shape, their cross-section reveals a complex layered texture from core to rim, composed of aggregates with different habits and morphologies. Figure 3c displays a section of such aggregates, evidencing an anhedral, massive core, overgrown by a ~150 µm thick layer made up of radially arranged, bladed crystals, defining a stockade-like structure. The inset of Figure 3c shows that, on the outside, these undergo a splitting and a loss of co-orientation, resulting in the formation of rosettes comprised of flat plates. The aggregate illustrated by Figure 3d, relative to the same experimental conditions but collected after one month after the first nucleation, shows the presence of an outer compact layer of ~10 mm thickness. It is worth noting the change in morphology undergone by the core of the aggregates occurred within the period of 15 days < h < one month, since Figure 3d reveals a core which is no longer massive, comprising subhedral crystals of apparently elongated shapes.

The second event of nucleation occurred after 360 h. Elongated crystals (Figure 2b) were observed, similar to those observed in experiments using low amounts of Na_2PO_4. However, in this case, the crystals lack pseudofacets and the equatorial cleft, and their faces are striated and bounded by rounded edges.

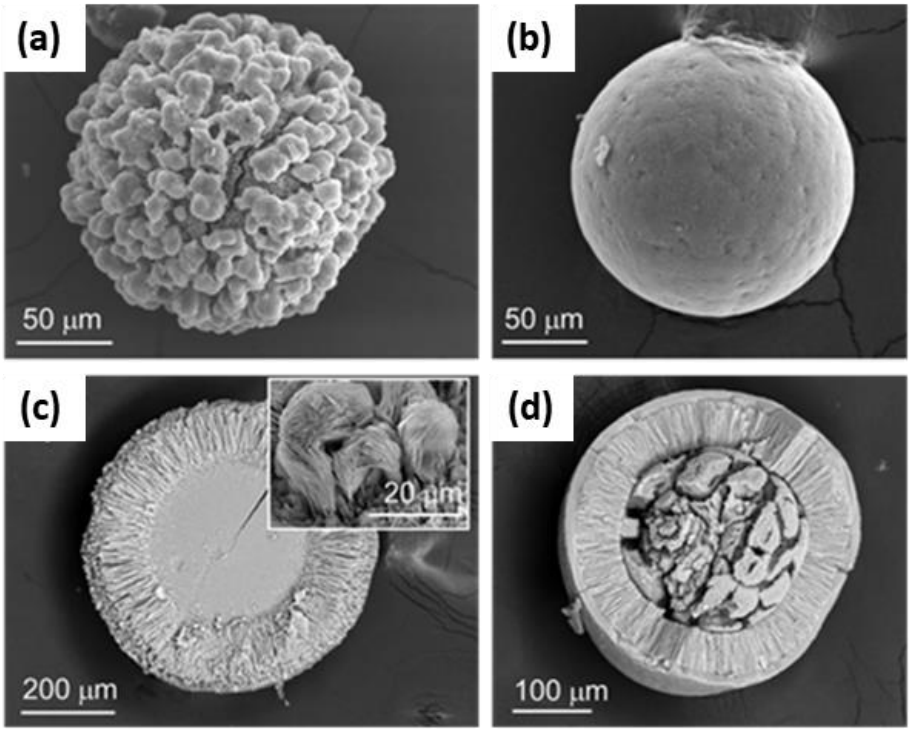

Figure 3. SEM micrographs of solids obtained from Mixture III after 15 days (**a**,**c**), and one month (**b**,**d**) after the first nucleation, respectively. The inset in (**c**) corresponds to a magnified micrograph over the layer of tabular, elongated crystals.

3.2. Raman Spectroscopy

The solids nucleated and grown in the present experiments frequently included aggregates displaying microscopic features, whose nature was suitably assessed with micro-Raman.

3.2.1. Inert Silica Gel Growth Experiments

Figure 4 shows the Raman spectra of the three different morphologies found in the P-free experiments. In the case of the rhombohedral crystals (Figure 4a), five bands have been identified. The three with the larger frequencies (1435, 1085 and 711 cm^{-1}) arise from the internal vibrations of the CO_3^{2-} groups contained in the crystal. The intense band (ν_1) corresponds to the symmetric stretching of the CO_3^{2-} group at 1085 cm^{-1}. The ν_2 (asymmetric deformation) vibration mode is not active in Raman. The values attributed to the ν_3 (asymmetric stretching) and ν_4 modes (symmetric deformation) are 1435 cm^{-1} and 711 cm^{-1}, respectively. Moreover, the principal Raman frequency ν_1 is accompanied by a satellite at 1067 cm^{-1} [46]. The observed vibrational bands fit to well-documented values of experimental and natural calcites [47,48]. The lower wavenumbers of calcite (280 and 155 cm^{-1}) observed in the spectrum arise from the external vibration of the CO_3^{2-} groups, which involves the translatory and rotator oscillations of those groups (relative translations between the cation and anionic group) [46]. A weak line observed at 1749 cm^{-1} may be regarded as the combination band of $\nu_1 + \nu_4$ [48].

The Raman spectrum of flat crystals showing the flower-like morphology can be seen in Figure 4b. In this case, only the frequencies corresponding to the ν_1 and ν_4 vibration modes are visible. A triplet of 1075–1081–1090 cm^{-1} can be observed with a high intensity in the ν^1 region, and another three lines of 677, 703 and 716 cm^{-1} arise in the ν_4 region. This spectrum is in good agreement with that of vaterite. The ν_2 and ν_3 bands were not detected, probably due to the presence of fluorescence and the weak intensities. In the low-frequency translational and rotational lattice region mode, nine Raman bands are observed. These vibrations, together with the triplet in the symmetric stretching region,

help to clearly differentiate this polymorph from calcite, which only has two bands at the low-frequency region. The presence of extra lattice modes is consistent with the large number of molecules in the unit cell (z = 12) of the vaterite crystals, compared with the lower number of molecules (z = 2) in the unit cell of the calcite crystal [49].

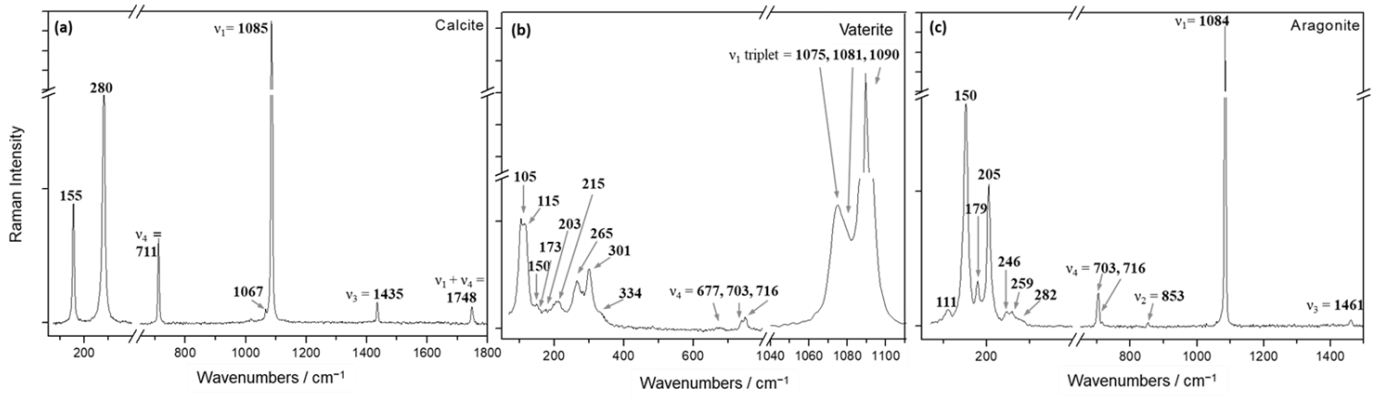

Figure 4. Raman spectra of crystals and aggregates obtained in the P-free experiments showing the characteristic bands for (**a**) calcite, (**b**) vaterite and (**c**) aragonite.

Finally, the Raman spectrum of the spherulitic aggregates can be seen in Figure 4c. The bands shown in this spectrum are consistent with aragonite. In the characteristic Raman spectrum of aragonite, the rotational and translational lattice modes appear in the low-frequency region (100–350 cm^{-1}), whereas the internal fundamental modes of vibration in the carbonate ions appear in the high-frequency region (600–1800 cm^{-1}). This spectrum is governed by the very strong Raman line (1085 cm^{-1}) attributed to the ν_1 symmetric stretching mode of the carbonate group. The ν_4 mode of CO_3^{2-} has values of 703 and 716 cm^{-1}. The ν_2 vibration mode is observed as a very weak band at 852 cm^{-1}; this vibrational mode is only permitted for the aragonite crystal structure. In the ν_3 region we were only able to observe a single band at 1461 cm^{-1}, rather than a doublet as reported by [50]. The low intensity bands in the region of 100–300 cm^{-1} arise from the translational and rotational modes of lattice vibration. The positions of the observed Raman bands agree with those reported by [51].

3.2.2. The 50 ppm P-Bearing Silica Gel Growth Experiments

In Figure 5a, the spectrum obtained after analyzing the elongated calcite crystals along the [100] direction can be observed. As shown, the spectrum exhibits characteristics very similar to those presented in the previous section for pure calcites, with the exception of the appearance of a new band, located at 965 cm^{-1}, near the symmetric stretching C-O ν_1 band. The detail of this band can be seen in Figure 5b. This figure shows the Raman band assigned to the P-O vibration located at 965 cm^{-1} for the calcite crystals obtained from experiments from Mixture II (P-bearing 50 ppm), recovered from the gel 15 days from the first nucleation event (in red), for crystals from the same Mixture II obtained one month after the first nucleation event (in black), and for calcite crystals obtained from experiments from Mixture III (P-bearing 500 ppm), recovered from gel 15 days after nucleation. As can be observed, there is a significant increase in the intensity of the band for the crystals grown with a higher amount of P in the medium (green band for 500 ppm crystals). The presence of this band can be attributed to the incorporation of PO_4^{3-} into the calcite structure.

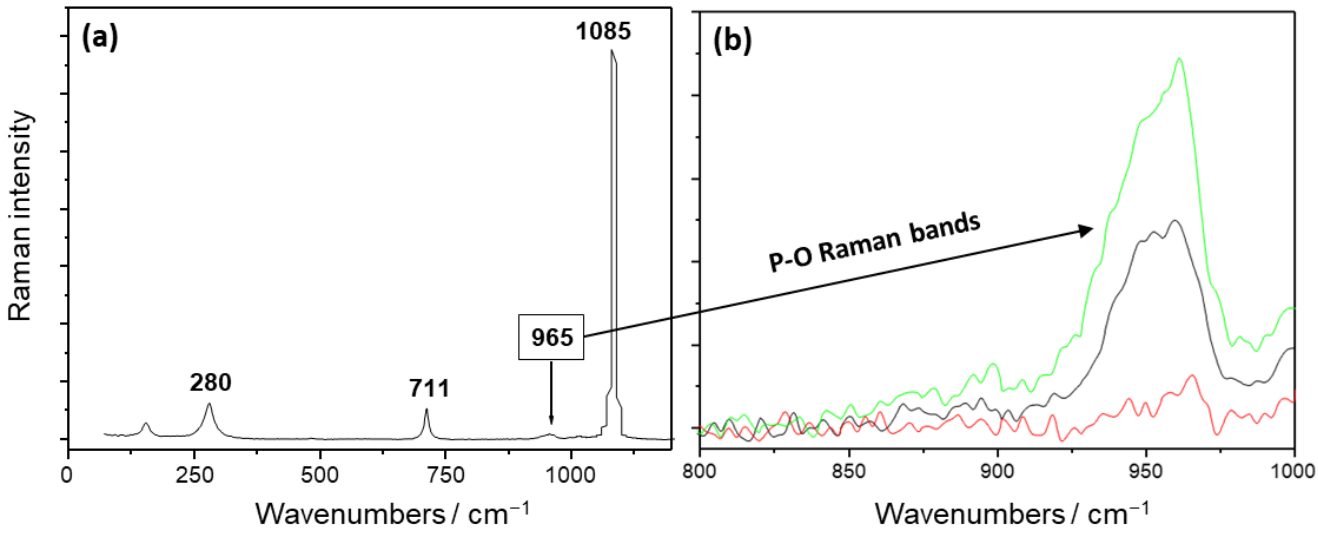

Figure 5. (**a**) Raman spectra of calcite crystals grown in the presence of phosphate. (**b**) Inset displaying the P-O Raman band area. The red line belongs to elongated calcite crystals from Mixture II (P-bearing 50 ppm), recovered from the gel 15 days after nucleation; the black line belongs to more elongated calcite crystals from same mixture, but recovered after one month of nucleation; and the green line corresponds to very elongated crystals from Mixture III (P-bearing 500 ppm), recovered from the gel 15 days after nucleation.

3.2.3. The 500 ppm P-Bearing Silica Gel Growth Experiments

Figure 6 displays Raman spectra targeting the core of the solid aggregates obtained in the experiment from Mixture III, 15 days and 30 days after the first nucleation. The comparison of the overall spectral profile in the 150 < cm^{-1} < 3400 shift range reveals a very similar set of peaks in the vicinities of 450, 600, 1000, 1450 and 2800 cm^{-1}, but with a decrease in peak broadening and noise, from 15 to 30 days. These spectrum modifications occur in tandem with the morphological variation shown in Figure 3b,c, from massive modifications to an intergrowth of subhedral crystal individuals.

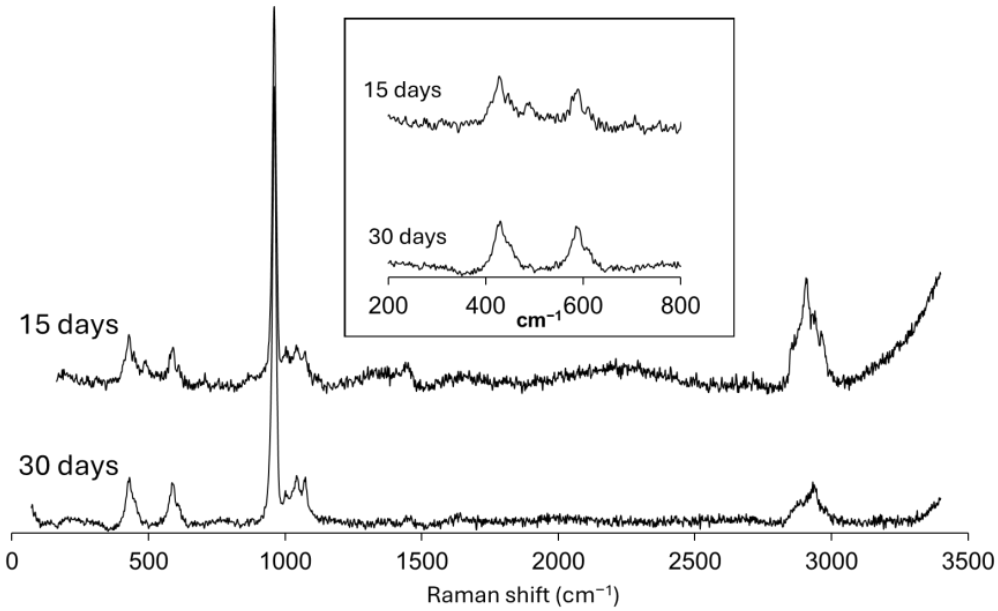

Figure 6. Raman spectra of the cores in the aggregates obtained in experiment III, after 15-day and 30-day diffusion times after the first nucleation.

Figure 7 shows the detailed spectral analysis of the Raman results, focusing on the cores of the spheres recovered from the gel 30 days after the first nucleation. For the band assignation concerning the vibrational modes of phosphate groups, we have relied on the work of [52–58], which suggest a good level of agreement with the overall spectra of octacalcium phosphate, $Ca_8(HPO_4)_2(PO_4)_4{\cdot}5H_2O$ (OCP), and/or hydroxyapatite, $Ca_5(PO_4)_3OH$ (HAP). The peaks in the 325 < cm^{-1} < 625 (Figure 7a) can be ascribed to the symmetric (ν_2) and (ν_4) antisymmetric bending vibrational modes of PO_4^{3-} groups at 430, 447 and 588, 610 cm^{-1}, respectively. Within the mentioned range, bands relative to the vibrational motions of HPO_4^{2-} occur, namely the symmetric ν_2 and antisymmetric ν_4 bending modes. Figure 7b reveals the band deconvolution performed in the 900 < cm^{-1} < 1100 interval, dominated by a very intense peak, ascribed to the symmetric stretching mode (ν_1) of PO_4^{3-} groups.

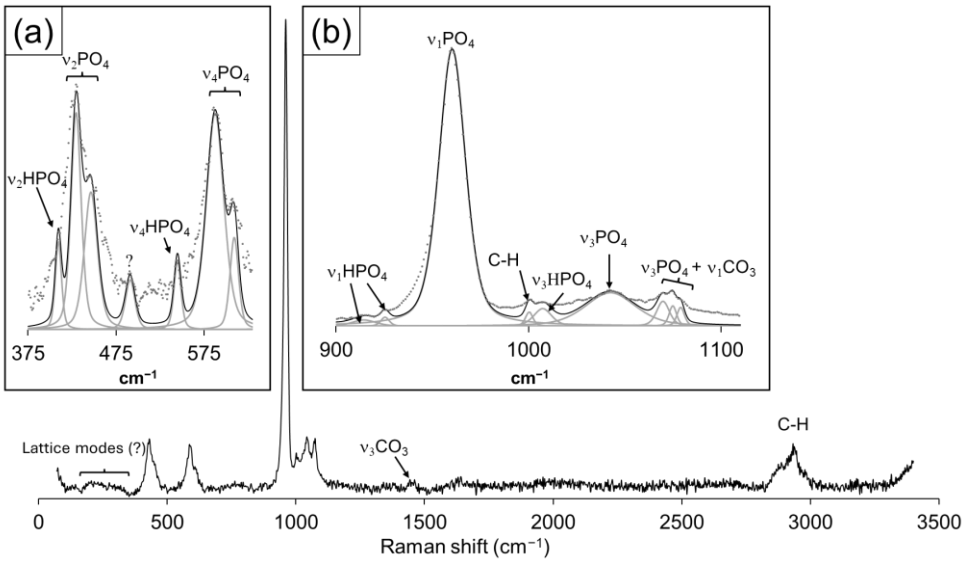

Figure 7. Raman spectra of a core from an aggregate obtained in experiment III, after 360 h of diffusion time. Insets display band deconvolutions and assignments for the spectral regions (**a**) 325 < cm^{-1} < 625, and (**b**) 900 < cm^{-1} < 1100. (See Table S1 in the Supplementary Information for the band assignments).

The peaks in the 325 < cm^{-1} < 625 (Figure 7a) can be ascribed to the symmetric (ν_2) and (ν_4) antisymmetric bending vibrational modes of PO_4^{3-} groups at 430, 447 and 588, 610 cm^{-1}, respectively. Within the mentioned range, bands relative to the vibrational motions of HPO_4^{2-} occur, namely the symmetric ν_2 and antisymmetric ν_4 bending modes. Figure 7b reveals the band deconvolution performed in the 900 < cm^{-1} < 1100 interval, dominated by a very intense peak, ascribed to the symmetric stretching mode (ν_1) of PO_4^{3-} groups. Though the remaining peaks in this interval are comparatively less intense and broad, it is possible to assign them to the antisymmetric stretching modes (ν_3) of PO_4^{3-} at 1043 and 1074 cm^{-1}, and the HPO_4^{2-} antisymmetric stretching mode (ν_3) at 1007 cm^{-1}. Regarding the latter phosphate group, the two low intensity peaks at 914 and 925 cm^{-1} may be attributed to its symmetric stretching mode ν_1. The remaining peaks within this shift interval cannot be ascribed to the vibrational characteristics of phosphate groups. The peak at 1000 cm^{-1} is attributable to the C-H bonds in apatite [59], with bands also occurring at 2876 and 2935 cm^{-1}, while CO_3^{2-} symmetric (ν_1) and antisymmetric (ν_3) stretching bands are observable at 1079 and 1451 cm^{-1}. The former mode is ascribed to carbonate groups in B-type apatite by [59], and the latter to the same anion in the structure of aragonite, $CaCO_3$ (Arg) [51]. It is worth noting that a low intensity, very broad hump spans the energy shifts in the 160 < cm^{-1} < 350 spectral region, where the lattice modes of vaterite, $CaCO_3$ (Vtr), may be found [51]. The variable Ca/P (~1.8–1.3) and high, also uneven, volatile content

(~60–40% of the total analysis by weight difference; see Table S4 in the Supplementary Information), revealed by multiple EMP analysis, strongly suggest the co-nucleation of calcium phosphate and carbonate phases at the core.

As Figure 8a,b reveal, band deconvolution is in good agreement with the reference information [52] regarding the vibrational modes of both PO_4^{3-} and HPO_4^{2-} in OCP and HAP, with the most intense peak at 959 cm^{-1}, displaying a shoulder towards 967 cm^{-1}. This spectral feature was determined by the latter author as being typical of the lower vibrational symmetry of the P-O stretching mode (ν_1) in the PO_4^{3-} group of OCP. In the 350 < cm^{-1} < 650 and 850 < cm^{-1} < 1100 regions, the bands corresponding to the symmetric and antisymmetric stretching (ν_1 and ν_3) and bending (ν_2 and ν_4) vibrational modes of PO_4^{3-} and HPO_4^{2-} occur, respectively. It is worth noting the development of intense peaks related to the vibration of HPO_4^{2-} groups, especially in the vicinity of 1010 cm^{-1}, where the antisymmetric stretching band is assigned (ν_3). The spectrum of these crystals is free from peaks related to the vibrations of carbonate groups, C-H, or O-H bonds (i.e., at shifts > 3000 cm^{-1}), and the general broadness of all peaks is an expression of low vibrational symmetry. The Ca/P ratio falls in the 1.6–1.8 range (see Table S4 in the Supplementary Information), possibly indicating some chemical inhomogeneity within these phases. Given the absence of spectral evidence for the occurrence of C-H, C-O, and O-H bonds, the ~20 wt%, lacking in analyses totals, may be attributed to the high porosity of the targeted areas (see SEM image inset in Figure 8).

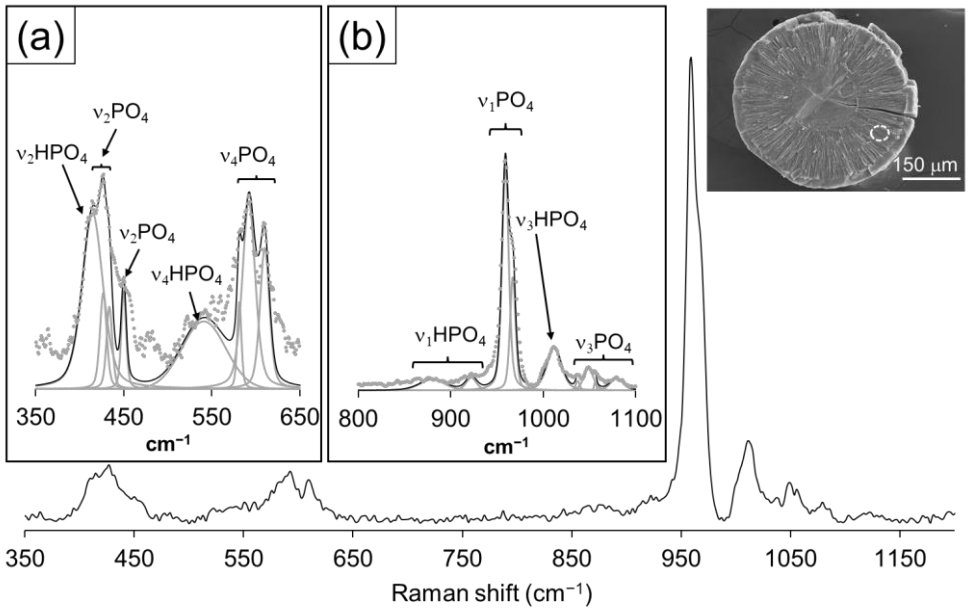

Figure 8. Raman spectra of the bladed crystals (see inset), from an aggregate obtained in experiment III 15 and 30 days after the first nucleation. Insets display band deconvolutions and assignments for the spectral regions (**a**) 350 < cm^{-1} < 650, and (**b**) 800 < cm^{-1} < 1200. (See Table S2 in the Supplementary Information for the band assignments).

Figure 9 reveals a representative Raman spectrum relative to the thin outermost growth layer of the aggregates, spanning the 100 < cm^{-1} < 3400 shift range. The overall spectral analysis results in the identification of PO_4^{3-} vibrational bands like those assigned to the Raman spectrum of the core, with slight differences focusing on the 925 < cm^{-1} < 1000 shift interval. In the 350 < cm^{-1} < 650 regions, the symmetric (ν_2) and antisymmetric (ν_4) bending modes of PO_4^{3-} can be assigned to the corresponding vibrations in the structures of both OCP and HAP, at 445 (ν_2) and 573, 590, and 607 cm^{-1} (ν_4), respectively. The O-P-O bending modes (ν_2) of PO_4^{3-} and the bending mode (ν_4) of the HPO_4^{2-} group in the structure of OCP, can be observed at 427 and 544 cm^{-1}, respectively. The 925 < cm^{-1} < 1000 shift range is dominated by a very intense peak at 960 cm^{-1}, ascribed to the symmetric

stretching modes (ν_1) of the PO_4^{3-} group in the structure of OCP/HAP, followed by broad peaks assigned to the antisymmetric stretching mode (ν_3) of PO_4^{3-} (1032, 1046, 1056 cm^{-1}), and the combination of the latter with the CO_3^{2-} symmetric stretching mode (ν_1) in the structure of HAP (1075 and 1070 cm^{-1}, respectively). A low intensity, broad peak of difficult interpretation in the vicinity of ~1010 cm^{-1} could be the expression of the ν_3 antisymmetric stretching mode of HPO_4^{2-} groups.

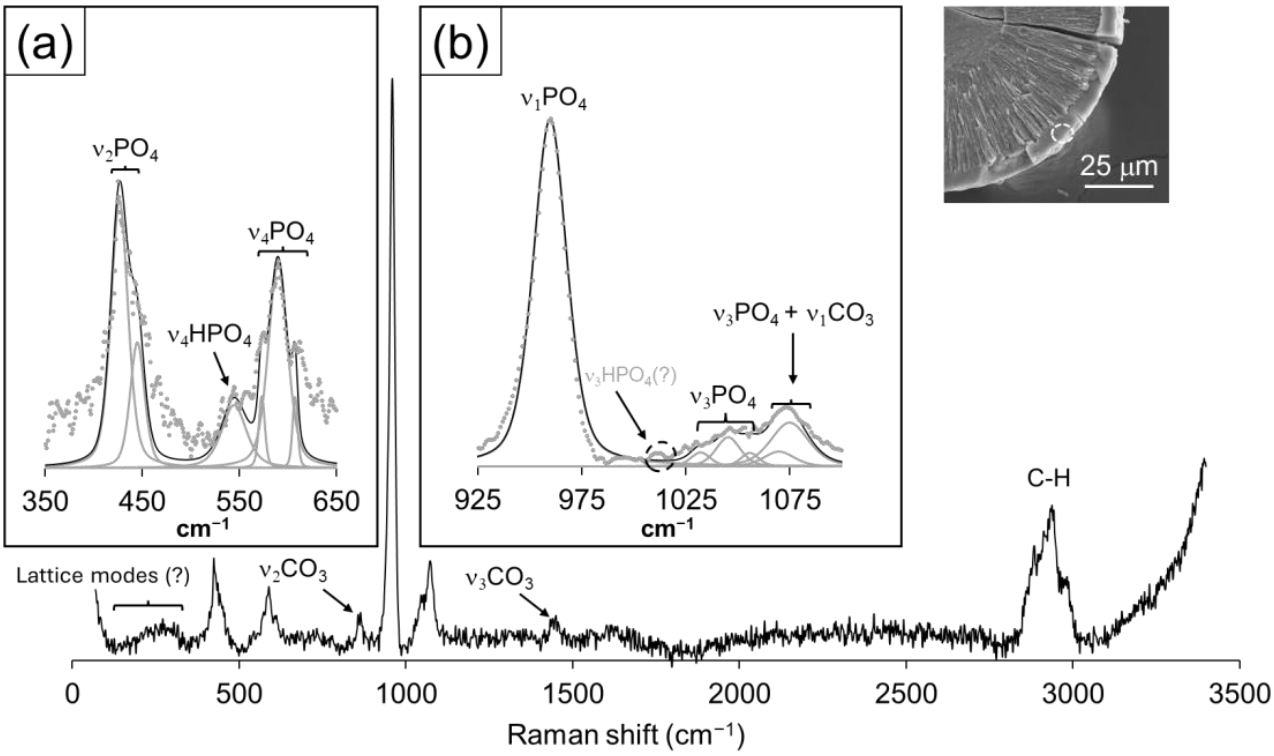

Figure 9. Raman spectra of the outermost growth layer (see inset) of an aggregate obtained from experiment III 30 days after the first nucleation. Insets display band deconvolutions and assignments for the spectral regions (**a**) 350 < cm^{-1} < 650, and (**b**) 925 < cm^{-1} < 1100. (See Table S3 in the Supplementary Information for the band assignments).

The peak in the vicinity of ~860 cm^{-1} can be assigned to the combination of the CO_3^{2-} symmetric bending (ν_2) modes at 856 and 865 cm^{-1}, and the broad peak at 1452 cm^{-1} to the antisymmetric stretching (ν_3) of the same anionic group, as observed for the structure of aragonite [51]. As observed for the core, the wide hump in the 160 < cm^{-1} < 350 spectral region could be the expression of vaterite lattice modes. It is worth mentioning the broad peak at ~2900 cm^{-1}, assigned to the vibrations of C-H bonds. Finally, the small thickness of this layer prohibited the reliable collection of Ca/P data.

The differences among the described Raman results can be very subtle, especially those concerning the core and the rim of the aggregates. Figure 10a shows a group comparison of the three spectra in the 350 < cm^{-1} < 650 region, where the main discrepancies lay in the development of HPO_4^{2-} vibrational bands. The spectral contrasts in the 985 < cm^{-1} < 1100 region, displayed in Figure 10b, are apparently more drastic, but harder to interpret, given the broad, low intense nature of peaks in this shift range. However, the main differences relate to the development of a ν_3 HPO_4^{2-} mode, the relative intensities of the ν_3 PO_4^{3-} bands in the structures of OCP and HAP, and the combination peak of ν_3 PO_4 + ν_1 CO_3^{2-} in HAP and the apatitic layers of OCP. The Raman spectrum of the bladed crystals offer the most striking variations with respect to core and rim growths. These correspond to the absence of a wide hump at low shifts, the absence of C-H modes, the inexistence/low expression of carbonate group vibrational bands, the higher intensity and better definition

of HPO_4^{2-} modes, and the absence of a rise in intensity for $cm^{-1} > 3200$, where O-H modes develop. These contrasts, their corresponding interpretation, and the discussion of the reactive pathway they reflect, will be discussed in the following section.

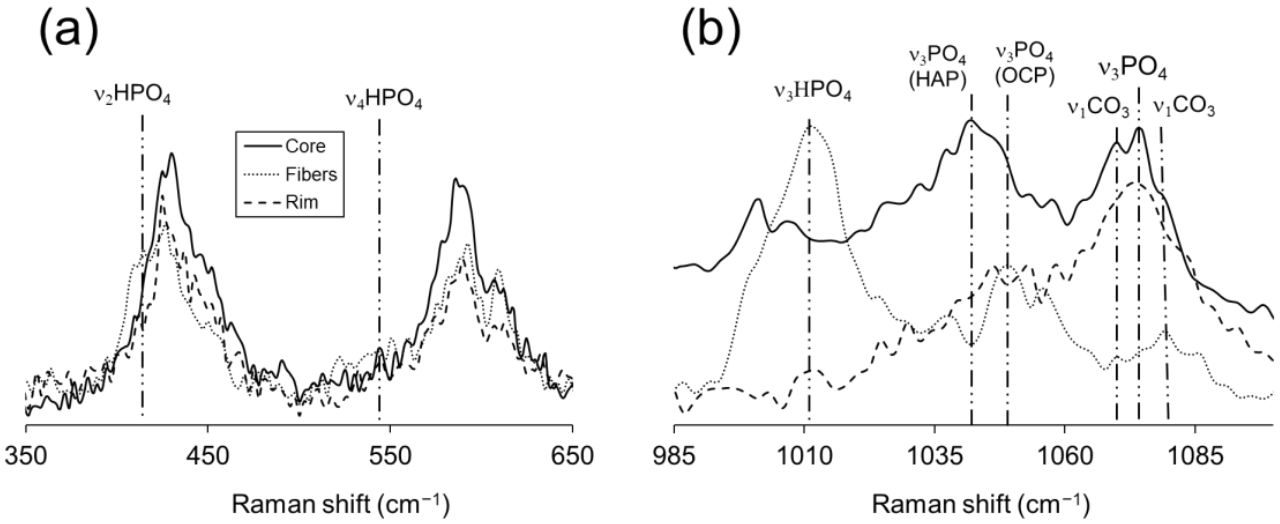

Figure 10. Raman spectra of core, fibers, and rim, of crystal aggregates obtained in experiment III, 30 days after the first nucleation, focusing on (**a**) $350 < cm^{-1} < 650$, and (**b**) $985 < cm^{-1} < 1100$ regions.

4. Discussion

4.1. Inert Silica Gel Growth Experiments

The three different morphologies shown in Figure 1, corresponding to three distinct $CaCO_3$ phases, appeared exclusively in experiments utilizing inert silica gel with reagents at identical concentrations. Two key factors account for the occurrence of these three $CaCO_3$ polymorphs within the same system. First, we begin with relatively high concentrations of Na_2CO_3 and $CaCl_2$, which consistently lead to elevated levels of supersaturation regarding the various $CaCO_3$ phases during nucleation, without reaching levels that result in catastrophic nucleation. Additionally, in dynamic systems such as crystal growth in gels, where reagent transport occurs via diffusion, supersaturation gradients develop along the gel column and evolve over time. Under these complex conditions, although calcite precipitates are the most abundant—logically so, as calcite is the stable phase under these temperature and pressure conditions—the concurrent metastable nucleation of the other two $CaCO_3$ polymorphs, aragonite and vaterite, remains consistently possible.

4.2. The Effect of Phosphate Ions on the Growth of Calcium Carbonate

The presence of phosphate in the aqueous media appears to be an important factor controlling the morphology of calcite. As mentioned in Section 3.2, the morphology of calcite crystals grown in the presence of phosphate differs greatly from those grown in its absence. While in the latter case, the crystals show the typical idiomorphic rhombohedral shape with hopper habit, the presence of phosphate in the aqueous media, even in a low concentration, leads to the appearance of a new crystal form, the acute rhombohedron {0221}, which gives calcite crystals a more elongated habit. Since Raman spectra analysis shows that phosphate is incorporated into the structure of calcite, we can conclude that the change in the habit is due to the incorporation/sorption of this anion in/on it. The modification of the habit of calcite crystals due to the presence of foreign ions in the crystallization medium has been extensively discussed in the literature [60,61]. It has been interpreted as the result of the preferential incorporation/adsorption of these ions onto certain faces other than those of the shape {1014}, which causes a significant lowering of their defect surface energies, thus stabilizing these faces relative to other faces [60]. Using atomistic simulations, these authors conclude that the presence of phosphates additives causes an elongation of calcite crystals due to the stabilization of the {1010}. These results differ from ours, but this may

be due to the fact that the two studies are hardly comparable. For example, in the study using atomistic simulations [60], only the equilibrium morphology was calculated, which may not correspond to that obtained in conditions far from the equilibrium, such as the conditions prevailing in a reaction diffusion system. Furthermore, no energy calculations of the form {0221} were performed, and only the effect of the HPO_4^{2-} species was considered in their calculations. Other authors have attributed the modification of the habit to a change in the calcite surface nanotopography, as a consequence of the differential interaction of the foreign ions with the steps on the calcite surfaces [61]. The authors demonstrate that this anisotropic interaction of the impurities with the rhombohedral form, to a more elongated shape, can occur by simply altering the orientation of the steps already available on the surface.

In any case, the stabilization of the {0221} form and the development of pseudofacets observed in our experiments is remarkably similar to that of calcite crystals grown in the presence of sulphate and chromate anions [15,62], and small cations such as Mg^{2+}, Co^{2+}, or Mn^{2+} [45].

4.3. Growth of Ca-Phosphates in the Presence of Carbonate Ions

4.3.1. Phase Identification

The early nucleation stages of experiment III most likely involved the formation of low crystalline phases, as evidenced from both the modifications in core morphology and Raman spectral characteristics from the 15 to 30 days of reaction times in the Results section. The nucleation of both amorphous calcium phosphate and carbonate precursors, with respect to the most thermodynamically stable phases of apatite and calcite/aragonite $CaCO_3$ polymorphs, respectively, is widely known in the literature [63–65]. The increase in crystallinity, reflected by the Raman spectra and the development of faces, reveals that, though already covered by an overgrowth of bladed crystals, the core of aggregates continued to mature towards a mixture of phases after 15 days of reaction times—one apatitic, the other a Ca carbonate. Such an apatitic phase displays the typical combination of bands for carbonate-apatite, as described by [52], with the addition of HPO_4^{2-} poorly defined vibrational modes. While the latter authors produced exclusively B-type carbonate apatite, where carbonate replaces for phosphate, the existence of C-H bonds and the spectral rise at >3300 cm^{-1} (O-H modes) could reflect the interaction between the HPO_4^{2-} and CO_3^{2-} groups in the A sites of apatite. An alternative interpretation could attribute these spectral peculiarities to the presence of a hydrated calcium carbonate; however, the Raman data suggest an intermediate between vaterite and aragonite polymorphs. The formula for type-B carbonated proposed by [66] would therefore not apply in the present case, due to the complex mutual replacements between PO_4^{3-}, HPO_4^{2-}, CO_3^{2-} and OH^- groups in both B and A-type sites.

The following growth layer of tabular and elongated crystals displays spectral characteristics typical of OCP, strikingly devoid of evidence for O-H bands, and little to no expression of the carbonate group vibrational modes. Furthermore, the obtained range of Ca/P ratios (1.6–1.8; see Table S4 in the Supplementary Information) are closer to that of apatite than OCP, with an excess Ca with respect to the ideal apatite formula. The acquired data do not allow for speculations around the type of ionic substitutions and related vacancies that enable such a composition. However, the incorporation of HPO_4^{2-} in Ca-deficient apatite proposed by [22] does not conform to the present results. We propose the occurrence of systematic structural inhomogeneities affecting these crystals, like the HAP-OCP nano-crystalline domains found by [31] in organic samples of osteocalcin. It is worth mentioning that the structures of OCP and apatite are very similar, with the former comprising apatitic Ca-PO_4 layers, bound together by a hydrated interlayer, where HPO_4^{2-} groups occur [29]. In fact, their epitactic intergrowth is governed by an excellent structural match along [001] in both minerals [30]. Figure 3c reveals the oriented growth of the tabular, elongated crystals, with the longest direction perpendicular to the interface with the preceding phase(s), indicating a structural affinity between substrate and overgrowth.

Finally, the curved nature of these crystals points towards the occurrence of structural strain in the reticular planes normal to the elongation, most likely induced by the inclusion of HPO_4^{2-} groups in the B and/or A sites of a deformed apatite, inheriting the structural characteristics of OCP. The fact that such *c*-axis is curved, and not jagged, also points towards a systematic change in the reticular parameters affecting the angular relationships among crystallographic axes.

The thin, outermost layer of the aggregates display a Raman spectrum very similar to the results gathered for the core, except for the poorly developed HPO_4^{2-} bands and better defined CO_3^{2-} modes, ascribed to the vibration of carbonate in the structure of aragonite. Though the resolution constraints preempted the determination of Ca/P ratios, the data are consistent with the presence of a carbonate-apatite with low HPO_4^{2-} contents, probably coexisting with aragonite.

It is worth noting that the Raman features displayed by calcium phosphate phases at both the core and rims, and the consequent non-stoichiometric compositions, strongly resembled those described for bioapatite [59]. However, in the present case, C-H vibrational modes are obviously unrelated to the presence of collagen in the grown phosphates.

4.3.2. Reaction Pathways

The nanoporous media in experiment III consists of a hydro-silica gel column, with 500 ppm of Na_2PO_4, and pH~5.5. Under such conditions and before the diffusion of the reactant solutions, the dominant phosphate species corresponds to $H_2PO_4^-$ [67]. The diffusing anion-bearing solution, with 0.5 M of Na_2CO_3, reaches a pH of ~9.8 following equilibration with atmospheric CO_2, and therefore the predominant carbonate-bearing species corresponds to HCO_3^- and CO_3^{2-}, with nearly equal distributions in a classic Bjerrum plot [68]. At the point of first nucleation, the pH conditions of the media should necessarily be in the range 5.5 << pH << 9.8, with the corresponding shift in the distribution of both the phosphate and carbonate-bearing species. Given the existence of both HPO_4^{2-} and PO_4^{3-} anionic groups in the HAP-like core phase of slightly matured samples (recovered 15 days after the first nucleation period), it is probable that such a solid does not correspond to the earliest nucleated phase, but rather to a recrystallized product of a primary, more protonated Ca phosphate (i.e., amorphous calcium phosphate, $Ca_xH_y(PO_4)_z{\cdot}nH_2O$). It is worth mentioning that the occurrence of non-stoichiometry in bioapatites has been a long-held discussion [69,70], with real measurements eluding the establishment of integer coefficients.

The static formation of an HAP-like phosphate at the core necessarily created an increasingly steep negative pH gradient over its surface, due to the decrease in the activities of dissociated phosphoric acid (HPO_4^{2-}) and OH- ions in the surrounding media. Under more acidic conditions, an epitactic growth of bladed, elongated crystals of a "pseudo" apatitic, HPO_4-rich, and OH-poor phase formed over the core substrate. Such an interpretation is also in agreement with the spectral data provided by [71,72], where the authors discovered "non-apatitic" PO_4^{3-} bands in FTIR spectra of bioapatites. The latter feature was also associated with the impossibility of assigning integer stoichiometric coefficients to biological apatites.

Similarly to what [73] described for the epitactic growth of brushite ($CaHPO_4{\cdot}2H_2O$) on gypsum cleavage surfaces, this structurally strained "pseudo" apatite could be metastable, and its heterogeneous nucleation over the core substrate facilitates the reduction in the nucleation energy barrier in response to structural affinities between both phases. Such acidic conditions did not enable the co-crystallization of a carbonate phase in this growth layer.

The continuous diffusion of an alkaline CO_3-bearing solution towards the nucleation sites, finally facilitated the nucleation of an HPO_4-poor CO_3-HAP, alongside an aragonitic $CaCO_3$ phase. Figure 11 displays X-ray elemental maps, regarding the distributions of both the Ca and P relative concentrations in the crystal aggregates obtained from experiment III. The relative concentration zoning reflects different growth pulses, from core to rim, induced not only by compositional changes (i.e., volatile content), but also morphology

and, consequently, porosity. For instance, though no gradual compositional, nor spectral variations were found in point analysis, the transition between the core and the overgrowing tabular crystals shown in Figure 11 appears to be characterized by a gradation in Ca and P concentrations. However, the most relevant chemical changes along this transition are the disappearance of a carbonate phase and little to no incorporation of OH/CO_3 groups in calcium phosphate, (i.e., lower volatile content). Finally, the analytical artifacts induced by the morphological change from a more massive core to the more porous epitactic layer of the elongated, bladed crystals, also needs to be accounted for in this transition.

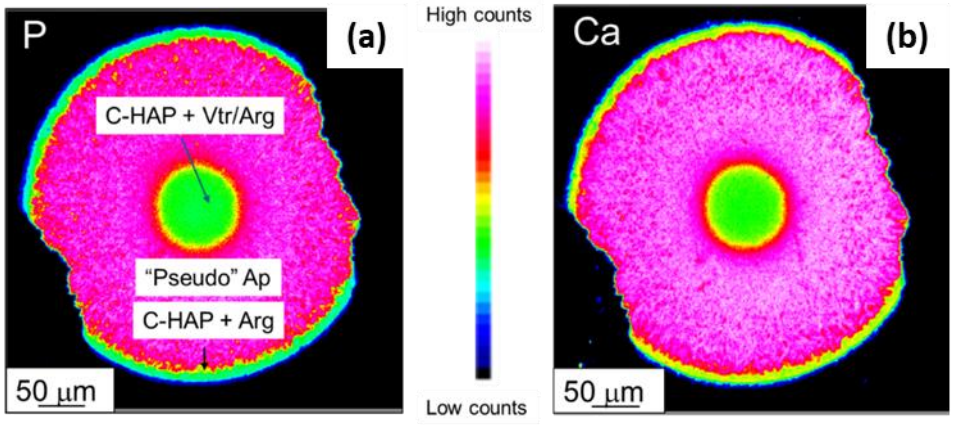

Figure 11. EMP X-ray elemental mapping of an aggregate collected in experiment III, 30 days after the first nucleation, regarding (**a**) calcium and (**b**) phosphorus. C-HAP = Carbonate-Hydroxyapatite, "Pseudo" Ap = "Pseudo" apatite, Arg = Aragonite, Vtr = Vaterite.

5. Conclusions

The growth of calcium carbonate in the presence of phosphate in the double diffusion system clearly affects the morphology of the calcite crystals, which exhibit the typical rhombohedral shape in the inert experiments and progressively become elongated along the c-axis as the P concentration increases in the gel medium, as a direct result of the incorporation of this anion. On the other hand, the growth of calcium phosphates in the presence of carbonate ions involves the sequential, heterogeneous nucleation of CO_3-bearing OCP/HAP-like phases, whose structural features are strongly controlled by the prevailing pH conditions and the existing structural similarities between each substrate and overgrowth. The obtained aggregates revealed Raman spectral characteristics very similar to those of bioapatites, produced here through strictly inorganic processes. Alongside the nucleation and growth of calcium phosphates, the saturation and pH conditions also facilitated the co-crystallization of $CaCO_3$ with vaterite/aragonite structures at the core and rim of aggregates. The obtained results underline the versatility of the experimental growth of crystals in gels as a method to simulate certain biomineralization processes, especially those involving carbonate and/or phosphate phases.

Supplementary Materials: The following supporting information can be downloaded at: https://www.mdpi.com/article/10.3390/cryst14070635/s1, Table S1. Raman band assignment for the core; Table S2. Raman band assignment for the fibers; Table S3. Raman band assignment for the rim; and Table S4. EMP.

Author Contributions: Conceptualization, N.S.-P.; Crystal growth experiments and SEM images, N.S.-P. and P.d.B.F.; Raman and EMP analyses, N.S.-P.; software, N.S-P., A.J.P. and J.M.A.; writing—original draft preparation, A.J.P. and N.S.-P.; writing—review and editing, A.J.P., N.S.-P. and J.M.A.; project administration, J.M.A.; funding acquisition, J.M.A. All authors have read and agreed to the published version of the manuscript.

Funding: This study was supported by the Ministry of Science and Innovation (Spain) under project PID2021-125467NB-I00.

Data Availability Statement: The raw data supporting the conclusions of this article will be made available by the authors on request.

Conflicts of Interest: The authors declare no conflicts of interest.

References

1. Ridgwell, A.; Zeebe, R.E. The role of the global carbonate cycle in the regulation and evolution of the Earth system. *Earth Planet. Sci. Lett.* **2005**, *234*, 299–315. [CrossRef]
2. Morse, J.W.; Mackenzie, F.T. *Geochemistry of Sedimentary Carbonates. Developments in Sedimentology*; Elsevier: Amsterdam, The Netherlands, 1990; p. 446.
3. Hua, B.; Deng, B.L.; Thorton, E.C.; Yang, J.; Amonette, J.E. Incorporation of chromate into calcium carbonate structure during coprecipitation. *Water Air Soil Pollut.* **2007**, *179*, 381–390. [CrossRef]
4. Tang, Y.Z.; Elzinga, E.J.; Lee, Y.J.; Reeder, R.J. Coprecipitation of chromate with calcite: Batch experiments and X-ray absorption spectroscopy. *Geochim. Cosmochim. Acta* **2007**, *71*, 1480–1493. [CrossRef]
5. Fernández-Díaz, L.; Fernández-González, A.; Prieto, M. The role of sulfate groups in controlling $CaCO_3$ polymorphism. *Geochim. Cosmochim. Acta* **2010**, *74*, 6064–6076. [CrossRef]
6. Fernández-Díaz, L.; Pina, C.M.; Astilleros, J.M.; Sánchez-Pastor, N. The carbonatation of Gypsum: Pathways and pseudomorph formation. *Am. Mineral.* **2009**, *94*, 1223–1234. [CrossRef]
7. Parker, S.C.; Titiloye, J.O.; Watson, G.W. Molecular modelling of carbonate minerals: Studies of growth and morphology. *Philos. Trans. R. Soc. Lond. A* **1993**, *344*, 37–44. [CrossRef]
8. Sangwal, K. *Additives and Crystallization Processes: From Fundamentals to Applications*; Wiley-Blackwell: Chichester, West Sussex, UK, 2007; p. 468.
9. Chernov, A.A. Growth of copolymer chains and mixed crystals trial-and-error statistics. *Soviet Physics Uspekhi.* **1970**, *13*, 101–128. [CrossRef]
10. Schosseler, P.M.; Wehrli, B.; Schweiger, A. Uptake of Cu^{2+} by the calcium carbonates vaterite and calcite as studied by continuous wave (cw) and pulse electron paramagnetic resonance. *Geochim. Cosmochim. Acta* **1999**, *63*, 1955–1967. [CrossRef]
11. Prieto, M.; Astilleros, J.; Fernández-Díaz, L. Environmental remediation by crystallization of solid solutions. *Elements* **2013**, *9*, 195–201. [CrossRef]
12. Astilleros, J.M.; Fernández-Díaz, L.; Putnis, A. The role of magnesium in the growth of calcite: An AFM study. *Chem. Geol.* **2010**, *271*, 52–58. [CrossRef]
13. Crocket, H.; Winchester, J.W. Coprecipitation of zinc with calcium carbonate. *Geochim. Cosmochim. Acta* **1966**, *30*, 1093–1109. [CrossRef]
14. Reeder, R.J.; Lamble, G.M.; Northrup, P.A. XAFS study of the coordination and local relaxation around Co^{2+}, Zn^{2+}, Pb^{2+}, and Ba^{2+} trace elements in calcite. *Am. Mineral.* **1999**, *84*, 1049–1060. [CrossRef]
15. Sánchez-Pastor, N.; Gigler, A.; Cruz, J.; Park, S.; Jordan, G.; Fernández-Díaz, L. Growth of calcium carbonate in the presence of Cr (VI). *Cryst. Growth Des.* **2011**, *11*, 3081–3089. [CrossRef]
16. Fernández-González, Á.; Fernández-Díaz, L. Growth of calcium carbonate in the presence of Se (VI) in silica hydrogel. *Am. Mineral.* **2013**, *98*, 1824–1833. [CrossRef]
17. Kohn, M.J.; Cerling, T.E. Stable isotope composition of Biological Apatite. *Rev. Min. Geochem.* **2002**, *48*, 455–488. [CrossRef]
18. Smith, S.C.; Douglas, M.; Moore, D.A.; Kukkadapu, R.V.; Arey, B.W. Uranium extraction from laboratory-synthesized, uranium-doped hydrous ferric oxides. *Environ. Sci. Technol.* **2009**, *43*, 2341–2347. [CrossRef]
19. Filippelli, G.M. The global phosphorous cycle: Past, present, future. *Elements* **2008**, *4*, 89–95. [CrossRef]
20. Elzinga, E.J.; Rouff, A.A.; Reeder, R.J. The long-term fate of Cu^{2+}, Zn^{2+}, and Pb^{2+} adsorption complexes at the calcite surface: An x-ray absorption spectroscopy study. *Geochim. Cosmochim. Acta* **2006**, *70*, 2715–2725. [CrossRef]
21. Kuczumow, A.; Blicharski, T.; Gorzelak, M.; Kosinski, J.; Lasota, A.; Gagala, J.; Nowak, J.; Jarzebski, M.; Jablonski, M. Measurements of energetic states resulting from ion exchanges in the isomorphic crystals of apatites and bioapatites. *Molecules* **2022**, *27*, 8913. [CrossRef]
22. Elliott, J.C. *Structure and Chemistry of the Apatites and Other Calcium Orthophosphates*, 1st ed.; Elsevier Science BV: Amsterdam, The Netherlands, 1994; p. 404.
23. Brown, W.E.; Smith, J.P.; Lehr, J.R.; Frazier, A.W. Cyrstallographic and chemical relations between octacalcium phosphate and hydroxyapatite. *Nature* **1962**, *196*, 1050–1054. [CrossRef]
24. Rey, C.; Hina, A.; Tofighi, A.; Glimcher, M.J. Maturation of poorly crystalline apatites: Chemical and structural aspects in vivo and in vitro. *Cells Mater.* **1995**, *5*, 345–356. [CrossRef]
25. Elliott, J.C. Calcium Phosphate Biominerals. *Rev. Min. Geochem.* **2002**, *48*, 427–453. [CrossRef]
26. Tung, M.S.; Brown, W.E. An intermediate state in hydrolysis of amorphous calcium phosphate. *Calcif. Tissue Int.* **1983**, *35*, 783–790. [CrossRef]
27. Montel, G.; Bonel, G.; Heughebaert, J.C.; Trombe, J.C.; Rey, C. New concepts in the composition, crystallization and growth of the mineral component of calcified tissues. *J. Cryst. Growth* **1981**, *53*, 74–99. [CrossRef]
28. Kay, M.I.; Young, A.R.; Posner, A.S. Crystal structure of hydroxyapatite. *Nature* **1964**, *204*, 1050–1052. [CrossRef] [PubMed]

29. Brown, W.E.; Eidelman, N.; Tomazic, B. Octacalcium phosphate as a Precursor in Biomineral Formation. *Adv. Dent. Res.* **1987**, *1*, 306–313. [CrossRef] [PubMed]
30. Fernández, M.E.; Zorrilla-Cangas, C.; García-García, R.; Asensio, J.A.; Reyes-Gasga, J. New model for the hydroxyapatite-octacalcium phosphate interface. *Acta Crystall. Sec. B Struct. Sci.* **2003**, *B59*, 175–181. [CrossRef] [PubMed]
31. Simon, P.; Grüner, D.; Worch, H.; Pompe, W.; Liche, H.; El Khassawna, T.; Heiss, C.; Wenisch, S.; Kniep, R. First evidence of octacalcium phosphate at osteocalcin nanocomplex as skeletal bone component directing collagen triple-helix nanofibril mineralization. *Sci. Rep.* **2018**, *8*, 13696. [CrossRef]
32. Miake, Y.; Shimoda, S.; Fukae, M.; Aoba, T. Epitaxial overgrowth of apatite crystals on the thin-ribbon precursor at early stages of porcine enamel mineralization. *Calcif. Tissue Int.* **1993**, *53*, 249–256. [CrossRef]
33. Rooji, J.F.; Nancollas, G.H. The formation and remineralization of artificial white spots lesions: A constant composition approach. *J. Dent. Res.* **1984**, *63*, 864–867. [CrossRef]
34. Nelson, D.G.A.; Wood, G.J.; Barry, J.C.; Featherstone, J.D.B. The structure of (100) defects in carbonates apatite crystallites: A high-resolution electron microscope study. *Ultramicroscopy* **1986**, *19*, 253–265. [CrossRef] [PubMed]
35. Iijima, M.; Moriwaki, Y. Lengthwise and oriented growth of octacalcium phosphate crystal in polyacryalamide gel in a model system of tooth enamel apatite formation. *J. Cryst. Growth* **1998**, *194*, 125–132. [CrossRef]
36. Falini, G.; Gazzano, M.; Ripamonti, A. Control of the architectural assembly of octacalcium phosphate crystals in denatured collagenous matrices. *J. Mater. Chem.* **2000**, *10*, 535–538. [CrossRef]
37. Grassmann, O.; Löbmann, P. Morphogenetic control of calcite crystal growth in sulfonic acid based hidrogels. *Chem. Eur. J.* **2003**, *9*, 1310–1316. [CrossRef] [PubMed]
38. Grassmann, O.; Löbmann, P. Biomimetic nucleation and growth of $CaCO_3$ in hydrogels incorporating carboxylate groups. *Biomaterals* **2004**, *25*, 277–282. [CrossRef]
39. Helbig, U. Growth of calcium carbonate in polyacrylamide hydrogel: Investigation of the influence of polymer content. *J. Cryst. Growth* **2008**, *310*, 2863–2870. [CrossRef]
40. Fernández-Díaz, L.; Putnis, A.; Prieto, M.; Putnis, C.V. The role of magnesium in the crystallization of calcite and aragonite in a porous medium. *J. Sediment. Res.* **1996**, *66*, 482–491. [CrossRef]
41. Prieto, M.; Putnis, A.; Fernández-Díaz, L. Crystallization of solid solutions from aqueous solutions in a porous medium: Zoning in (Ba, Sr), SO_4. *Geol. Mag.* **1993**, *130*, 289–299. [CrossRef]
42. Prieto, M.; Putnis, A.; Fernández-Díaz, L.; López-Andrés, S. Metastability in diffusing-reacting systems. *J. Cryst. Growth* **1994**, *142*, 225–235. [CrossRef]
43. Wojdyr, M. Fityk: A general-purpose peak fitting program. *J. Appl. Cryst.* **2010**, *43*, 1126–1128. [CrossRef]
44. KrystalShaper V1.5.0 © JCrystalSoft. 2018. Available online: http://www.jcrystal.com/products/krystalshaper/ (accessed on 29 September 2019).
45. Fernández-Díaz, L.; Astilleros, J.M.; Pina, C.M. The morphology of calcite crystals grown in a porous medium doped with divalent cations. *Chem. Geol.* **2006**, *225*, 314–321. [CrossRef]
46. Krishnamurti, D. The Raman spectrum of calcite and its interpretation. *Proc. Indian. Acad. Sci. Sect. A* **1957**, *46*, 183–202. [CrossRef]
47. Buzgar, N.; Apopei, A.I. The Raman study on certain carbonates. *Analele Stiintifice ale Universitatii "Al. I. Cuza"—Iasi* **2009**, *55*, 97–112.
48. Gunasekaran, S.; Anbalagan, G.; Pandi, S. Raman and infrared spectra of carbonates of calcite structure. *J. Raman Spect.* **2006**, *37*, 892–899. [CrossRef]
49. Gauldie, R.W.; Sharma, S.K.; Volk, E. Micro-raman spectral study of vaterite and aragonite otoliths of the coho salmon, Oncorhynchus kisutch. *Comp. Biochem. Physiol. Part A Physiol.* **1997**, *118*, 753–757. [CrossRef]
50. Couture, J.P.M. Anisotropy of the Raman effect in cubic crystals; theoretical study. *C. R. Hebd. Seances Acad. Sci.* **1947**, *224*, 902–904.
51. Urmos, J.; Sharma, S.K.; Mackenzie, F.T. Characterization of some biogenic carbonates with Raman spectroscopy. *Am. Mineral.* **1991**, *76*, 641–646.
52. Koutsopoulos, S. Synthesis and characterization of hydroxyapatite crystals: A review study on the analytical methods. *J. Biomed. Mater. Res.* **2002**, *62*, 600–612. [CrossRef]
53. Penel, G.; Leroy, N.; van Landuyt, P.; Flautre, B.; Hardouin, P.; Lemaître, J.; Leroy, G. Raman microspectrometry studies of brushite cement: In vivo evolution in a sheep model. *Bone* **1999**, *25* (Suppl. 1), 81S–84S. [CrossRef]
54. de Aza, P.N.; Guitian, F.; Santos, C.; de Aza, S.; Cusco, R.; Artus, L. Vibrational investigation of calcium phosphate compounds. 2. Comparison between hydroxyapatite and β-tricalcium phosphate. *Chem. Mater.* **1997**, *9*, 916–922. [CrossRef]
55. Sauer, G.R.; Zunic, W.B.; During, J.R.; Wuthier, R.E. Fourier transform Raman spectroscopy of synthetic and biological calcium phosphates. *Calcif. Tissue Int.* **1994**, *54*, 414–420. [CrossRef] [PubMed]
56. Tsuda, H.; Arends, J. Raman spectra of human dental calculus. *J. Dent. Res.* **1993**, *72*, 1609–1613. [CrossRef] [PubMed]
57. O'Shea, D.C.; Bartlett, M.L.; Young, R.A. Compositional analysis of apatites with laser-Raman spectroscopy: (OH, F, Cl) apatites. *Arch. Oral Biol.* **1974**, *19*, 995–1006. [CrossRef] [PubMed]
58. Griffith, W.P. Raman studies of rock-forming minerals. *Part II. Minerals containing MO3, MO4, and MO6 groups. J. Chem. Soc. (A)* **1970**, *0*, 286–291. [CrossRef]
59. Awonusi, A.; Morris, M.D.; Tecklenburg, M.M.J. Carbonate assignment and calibration in the Raman spectrum of apatite. *Calcif. Tissue Int.* **2007**, *81*, 46–52. [CrossRef]

60. Titiloye, J.O.; Parker, S.C.; Mann, S.J. Atomistic simulation of calcite surfaces and the influence of growth additives on their morphology. *J. Cryst. Growth* **1993**, *131*, 533–545. [CrossRef]
61. Davis, K.J.; Dove, P.M.; Wasylenki, L.E.; De Yoreo, J.J. Morphological consequences of differential Mg^{2+} incorporation at structurally distinct steps on calcite. *Am. Mineral.* **2004**, *89*, 714–720. [CrossRef]
62. Mayorga, I.C.; Astilleros, J.M.; Fernández-Díaz, L. Precipitation of $CaCO_3$ Polymorphs from Aqueous Solutions: The Role of pH and Sulphate Groups. *Minerals* **2019**, *9*, 178. [CrossRef]
63. Addadi, L.; Joester, D.; Nudelman, F.; Weiner, S. Mollusk shell formation: A source of new concepts for understanding biomineralization processes. *Chem. Eur. J.* **2006**, *12*, 980–987. [CrossRef]
64. Veis, A.; Dorvee, J.R. Biomineralization Mechanisms: A New Paradigm for Crystal Nucleation in Organic Matrices. *Calcif. Tissue Int.* **2013**, *93*, 307–315. [CrossRef]
65. Bachra, B.N.; Trautz, O.R.; Simon, S.L. Precipitation of calcium carbonates and phosphates. I. Spontaneous precipitation of calcium carbonates and phosphates under physiological conditions. *Arch. Biochem. Biophys.* **1963**, *103*, 124–138. [CrossRef]
66. Rey, C.C.; Combes, C.; Drouet, C. Synthesis and physical chemical characterizations of octacalcium phosphate-based biomaterials for hard-tissue regeneration. In *Octacalcium Phosphate Biomaterials: Understanding of Bioactive Properties and Application*, 1st ed.; Suzuki, O., Insley, G., Eds.; Woodhead Publishing Series in Biomaterials; Elsevier: Amsterdam, The Netherlands, 2019; pp. 177–212. [CrossRef]
67. Havlin, J.L.; Schlegel, A.J. Review of phosphite as a plant nutrient and fungicide. *Soil Syst.* **2021**, *5*, 52. [CrossRef]
68. Zeebe, R.E.; Wolf-Gladrow, D.A. *CO_2 in Seawater: Equilibrium, Kinetics, Isotopes*; Elsevier: Amsterdam, The Netherlands, 2001; 346p.
69. Legros, R.; Balmain, N.; Bonel, G. Age-related changes in mineral of rat and bovine cortical bone. *Calcif. Tissue. Int.* **1987**, *41*, 137–144. [CrossRef]
70. Kuczumow, A.; Gorzelak, M.; Kosiński, J.; Lasota, A.; Blicharski, T.; Gągała, J.; Nowak, J.; Jarzębski, M.; Jabłoński, M. Hierarchy of Bioapatites. *Int. J. Mol. Sci.* **2022**, *23*, 9537. [CrossRef]
71. Omelon, S.J.; Grynpas, M.D. Relationships between polyphosphate chemistry, biochemistry and apatite biomineralization. *Chem. Rev.* **2008**, *108*, 4694–4715. [CrossRef]
72. Rey, C.; Collins, B.; Goehl, T.; Dickson, I.R.; Glimcher, M.J. The carbonate environment in bone mineral: A resolution-enhanced fourier transform infrared spectroscopy study. *Calcif. Tissue Int.* **1989**, *45*, 157–164. [CrossRef]
73. Pinto, A.J.; Jiménez, A.; Prieto, M. Interaction of phosphate-bearing solutions with gypsum: Epitaxy and induced twinning of brushite ($CaHPO_4 \cdot 2H_2O$) on the gypsum cleavage surface. *Am. Mineral.* **2009**, *94*, 313–322. [CrossRef]